

## Structure-independent flat bands induced by discontinuity plasma-air interface in photonic crystals

Xin Ye,<sup>1</sup> Yongge Wang,<sup>1</sup> Jingfeng Yao<sup>1,2,\*</sup>, Ying Wang,<sup>1,2</sup> Chengxun Yuan<sup>1,2,†</sup> and Zhongxiang Zhou<sup>1,2,‡</sup>

<sup>1</sup>*School of Physics, Harbin Institute of Technology, Harbin 150001, People's Republic of China*

<sup>2</sup>*Heilongjiang Provincial Key Laboratory of Plasma Physics and Application Technology, Harbin 150001, People's Republic of China*



(Received 3 February 2023; revised 30 April 2023; accepted 2 May 2023; published 9 May 2023)

The band structures of transverse electric (TE) polarized dispersive photonic crystals are generally more complicated than those of transverse magnetic (TM) polarized photonic crystals. Here, by simplifying the governing equations of a TE polarized dispersion system and conducting the band structure analysis, we deduce the Hermitian eigenstates of the vector electric field. The results exhibit the double degeneracy eigenstates in the triangular lattice for lower eigenfrequencies and numerous plasmon-induced flat band modes in the interface of the plasma and air for higher eigenfrequencies. Moreover, we illustrate that the surface plasmon modes tend to present the quantized eigenfrequencies, which is due to the boundary condition imposed by the cylindrical geometry. However, when the eigenfrequency approaches the surface plasma frequency, the localization of the field on the boundary becomes stronger, which weakens the coupling between sites and reduces the dependence of the flat bands on the lattice structure. Unlike the generation mechanism of the lattice-induced flat bands, such plasma frequency-dependent localization at the interface enables a robust flat band characteristic immune to the lattice disorder and provides a novel degree of freedom to control the energy band. Our findings are expected to be useful for electromagnetic wave manipulation and field enhancement.

DOI: [10.1103/PhysRevB.107.195301](https://doi.org/10.1103/PhysRevB.107.195301)

### I. INTRODUCTION

A rich variety of intriguing phenomena in solid-state physics, including unusual ferromagnetic ground state [1], superconductivity [2], *Zitterbewegung* [3], and pseudodiffusive transmission [4], are generally attributed to the characteristics of electron transport and localization in diverse matters [5,6]. Numerous efforts have been made to understand these mechanisms within the photonic community of optical waveguide [7] and various metamaterials [8]. As one class of such systems, photonic crystals support the electromagnetic wave to propagate and refabricate their dispersion relations, allowing us to optically explore band structure [9–11]. The early work of photonic crystals thrived from dispersiveless materials with constant permittivities [12,13], and now it is further developing towards temporal and spatial dispersive systems with frequency-dependent electromagnetic properties [14–17]. However, frequency-dependent permittivities usually lead to nonlinear eigenvalue problems in the transverse electric (TE) polarization case [18,19]. Importantly, both band structure and field distribution in such nonlinear systems can show attractive electromagnetic response characteristics, which are typically endowed with Dirac cone with linear spectrum and numerous flat bands or quasiflat bands with zero groups velocity.

The band structure of graphene near the corner of the Brillouin zone at the K point can be described by the massless Dirac equation and hence exhibit the linear dispersion [20,21]. The typical linear dispersion behavior is entirely originated from the threefold rotational symmetry of the graphene lattice in condense state physics. The existence of Dirac cone dispersion is not limited to electronic models but can also be found in many other photon platforms [22–24]. It is well known that the classical wave periodic systems with spatial potentials of the same symmetry can generate Dirac spectra, which is determined by the system structure. Contrary to atomic systems, for dispersive metallic or plasma photonic crystal systems, Dirac cones are observed in triangular lattices rather than in honeycomb lattices [25,26]. In fact, the physical mechanism of the linear dispersions of a Dirac cone in photonic crystals described by the Drude model is not well explicated.

On the other hand, the singular characteristics of the dispersiveless flat band have been widely investigated in a variety of platforms, including ultracold atoms [27], metamaterials [28], photonic crystals [29], electronic, and other realistic materials, which mimic the flat-band properties in condensed matter systems [30]. The kinetic energy in a flat band is completely quenched, which suppresses wave transport and then enhances the particle interaction, leading to strongly correlated systems [31,32]. Due to the strong localized field, the fabricated flat bands are useful for potential applications such as diffraction-free image transmission [33], Aharonov-Bohm photonic cages [34], lasing [35], Raman scattering [36], and nonlinear optics [37]. Hence, it is meaningful to study the formation mechanism of photonic flat bands. Generally, the

\*yaojf@hit.edu.cn

†yuancx@hit.edu.cn

‡zhouzx@hit.edu.cn

dispersiveless photonic crystals offer a high control over the lattice geometry and allow for the addition of tunable disorder or interactions between the sites. However, it is notable that the dependence on the structure of the flat bands in dispersive photonic crystals is still yet to be explored. Compared to geometrically induced flat bands, which cause nonzero dispersion when subjected to external disturbances [38], in plasma photonic crystals, the localized surface modes at the plasma-air interface are less affected by external disturbances. Therefore, the research on the flat bands in the dispersive system offers a promising tool for optically probe zero group velocity, high density of states (DOS), and infinite effective mass [39–41].

In this paper, we formulate the coupling eigenequation in TE polarized photonic crystals with Drude dispersion. Then the energy band and eigenmodes of typical triangular and honeycomb lattices are numerically investigated. For the low-frequency range, we exploit the  $\mathbf{k} \cdot \mathbf{p}$  theory to derive the linear dispersion for the triangular lattice and calculate its relative slope. Furthermore, the formation mechanism of the flat bands for higher eigenmodes is also presented. Finally, we extensively discuss the surface plasmon modes at the discontinuity plasma-air interface and show the structure-independent flat bands characteristics.

## II. MODEL AND METHOD

In the case of the isolated plasma columns periodically embedded in the air host, we consider the linear electromagnetic response of free electron under weak excitation. The equations of motion for an electron with mass  $m$  and charge  $e$ , located at a position  $\mathbf{r}$ , damped by a electron-neutral interaction with a collision frequency  $\nu$ , and subject to an electric field  $\mathbf{E}$  are as follows:

$$m \frac{d^2 \mathbf{r}}{dt^2} = -e\mathbf{E} - m\nu \frac{d\mathbf{r}}{dt}. \quad (1)$$

Note that the current density  $\mathbf{J}$  is related to  $d\mathbf{r}/dt$  as  $\mathbf{J} = -en_e d\mathbf{r}/dt$  with  $n_e$  being the electron density. We reformulate Eq. (1) as follows:

$$\frac{\partial \mathbf{J}}{\partial t} = \varepsilon_0 \omega_{pe}^2 \mathbf{E} - \nu \mathbf{J}, \quad (2)$$

where  $\omega_{pe}(\mathbf{r}) = \sqrt{e^2 n_e(\mathbf{r}) / \varepsilon_0 m}$  resembles the distribution of plasma frequency with  $\varepsilon_0$  being the permittivity of the free space. The introduction of  $\mathbf{J}$  results in a first-order derivative in time. In general, the electromagnetic field is described by Maxwell's equations:

$$\frac{\partial \mathbf{H}}{\partial t} = -\frac{1}{\mu_0} \nabla \times \mathbf{E}, \quad (3)$$

$$\frac{\partial \mathbf{E}}{\partial t} = \frac{1}{\varepsilon_0} (\nabla \times \mathbf{H} - \mathbf{J}). \quad (4)$$

Here  $\mathbf{H}$  is the magnetic field and  $\mu_0$  is the vacuum permeability. Then we assume that all fields with the time-dependent term  $e^{i\omega t}$  in the Maxwell's equations satisfy the following

eigensystem:

$$\omega \begin{pmatrix} \mathbf{H} \\ \mathbf{E} \\ \mathbf{J} \end{pmatrix} = \begin{pmatrix} 0 & \frac{i}{\mu_0} \nabla \times & 0 \\ \frac{-i}{\varepsilon_0} \nabla \times & 0 & \frac{i}{\varepsilon_0} \\ 0 & -i\omega_{pe}^2 \varepsilon_0 & i\nu \end{pmatrix} \begin{pmatrix} \mathbf{H} \\ \mathbf{E} \\ \mathbf{J} \end{pmatrix}. \quad (5)$$

To get the real eigenvalues  $\omega$ , a lossless Drude model is adopted by applying  $\nu = 0$ . In fact, not all field vectors are necessary, so we further reduce Eq. (5) to the following matrix form:

$$\omega^2 \begin{pmatrix} \mathbf{H} \\ \mathbf{E} \\ \mathbf{J} \end{pmatrix} = \begin{pmatrix} c^2 \nabla \times \nabla \times & 0 & -c^2 \nabla \times \\ 0 & \omega_{pe}^2 + c^2 \nabla \times \nabla \times & 0 \\ \omega_{pe}^2 \nabla \times & 0 & \omega_{pe}^2 \end{pmatrix} \begin{pmatrix} \mathbf{H} \\ \mathbf{E} \\ \mathbf{J} \end{pmatrix}, \quad (6)$$

where  $c = 1/\sqrt{\varepsilon_0 \mu_0}$  is the speed of light in the vacuum. Thus, one can derive electromagnetic field equations for the generalized  $\mathbf{E}$  or  $(\mathbf{H}, \mathbf{J})^T$  wave function involving a second-order time derivative. For instance, for the  $\mathbf{E}$  component in the TE mode case,

$$\omega^2 \begin{pmatrix} E_x \\ E_y \end{pmatrix} = \begin{pmatrix} \omega_{pe}^2 - c^2 \frac{\partial^2}{\partial y^2} & c^2 \frac{\partial^2}{\partial x \partial y} \\ c^2 \frac{\partial^2}{\partial x \partial y} & \omega_{pe}^2 - c^2 \frac{\partial^2}{\partial x^2} \end{pmatrix} \begin{pmatrix} E_x \\ E_y \end{pmatrix}, \quad (7)$$

where  $(E_x, E_y)^T$  is the time-harmonic eigenmode. Obviously, Eq. (7) is a Hermitian eigenvalue problem. Moreover, the Hermitian nature of the operator in Eq. (7) ensures that the eigenfunctions of the system form a complete, orthonormal basis.

Then we can find the following orthogonality condition in terms of the physical fields:

$$\int d\mathbf{r} (E_{x,m}^* E_{x,n} + E_{y,m}^* E_{y,n}) = \delta_{mn}. \quad (8)$$

Here the subscripts  $m$  and  $n$  represent the index of basis.  $\delta_{mn}$  is the Kronecker symbol. Note that the orthogonality relation is frequency independent and thus efficient for the dispersive photonic crystal system with plasma permittivity.

We now perform the photonic band structure analysis in three kinds of photonic crystal structures. One plasma site in the unit cell for the triangular lattice [as shown in the left in Fig. 1(a)], two plasma sites with different plasma frequency for hybrid lattice [as shown in the middle in Fig. 1(a)] and two same plasma sites for honeycomb lattice [as shown in the right in Fig. 1(a)]. The periodic structures consist of the plasma columns ( $\omega_{pe} = \omega_{p0}$ ) of radii  $r = 0.2a$  embedded in the air host ( $\omega_{pe} = 0$ ). As shown in Fig. 1(a), the color of the circle represents the value of the plasma frequency. The blue circles represent  $\omega_{p0}a/2\pi c = 2$  and white circles represent  $\omega_{p0}a/2\pi c = 0$ . For the purple circles in the middle in Fig. 1(a),  $\omega_{p0}a/2\pi c = 1$ . Figure 1(b) presents the TE band structures in the first Brillouin zone for the three corresponding lattices, respectively. To calculate the band structure, we use a finite-difference discretization of the transverse electric field components  $E_x$  and  $E_y$  with a Yee grid in a single unit cell [18]. Consequently, the numerical band computation naturally converts into an eigenvalue problem for finite-difference matrix. The matrix elements at the boundaries are determined by

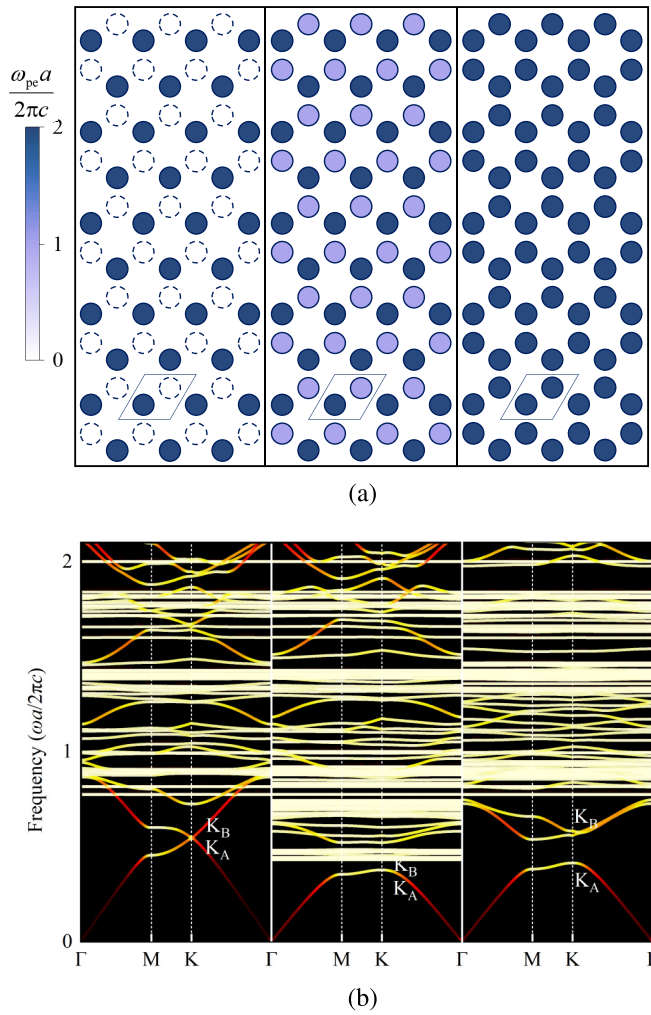


FIG. 1. (a) The photonic crystal structures from (left) triangular lattice to (right) honeycomb lattice, which consist of plasma columns embedded in the air host, with column radius  $r/a = 0.2$  and varied plasma frequency  $\omega_{pe}a/2\pi c$ , where  $a$  is the lattice constant. The middle panel represents a lattice structure composed of plasma columns with two different plasma frequencies. The blue circles represent  $\omega_{p0}a/2\pi c = 2$  and white circles represent  $\omega_{p0}a/2\pi c = 0$ . For the purple circles in the middle,  $\omega_{p0}a/2\pi c = 1$ . (b) The corresponding TE bands of the first Brillouin zones for three structures showed in (a), and the darker color of the curve represents higher group velocity. Points  $K_A$  and  $K_B$  are the lowest and second-lowest modes at the K point, respectively.

the Bloch's theorem, which retains Hermitian of the matrix operators.

As presented in the left plot of Fig. 1(b), for the triangular-lattice photonic crystal, the first lowest and second-lowest TE eigenmodes ( $K_A$  and  $K_B$ ) are degenerate at the K point. It shows that there is a Dirac cone in the energy band structure. This is quite similar to the tight-binding electron in graphene. As for the honeycomb lattice as shown in the right plot of Fig. 1(b), the degeneracy at the Dirac cone is lifted, opening a photonic band gap. Specifically, the second band is clearly separated from the first band at K, whereas the former are also in contact with the third band. Since the plasma is adopted as the lattice site as shown in Fig. 1, which is opaque to

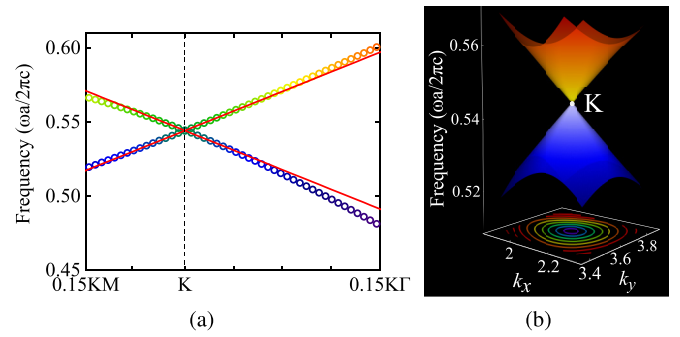


FIG. 2. TE band structure near K point for the triangular lattice of plasma columns embedded in the air host, with column radius  $r/a = 0.2$  and plasma frequency  $\omega_{p0}a/2\pi c = 2$ , where  $a$  is the lattice constant. (a) The circles are extracted from Fig. 1(b) and the red curves show the results predicted by Eq. (A17). (b) The isotropic Dirac cone at K point in the quasimomentum space.

the electromagnetic waves and is described by the Drude model. Thus, the lattice site in Fig. 1 is equivalent to the potential barrier, and the host corresponds to the potential well. Therefore, the triangular lattice mimics the honeycomb atomic structure with a Dirac cone (Fig. S2 in the Supplemental Material [42]), while the honeycomb lattice corresponds to the triangular atomic structure with the band gap (Fig. S3 in the Supplemental Material [42]). Meanwhile, for these two lattices, numerous flat bands with nearly zero group velocity are observed in the TE band diagrams, which correspond to the surface plasmon modes in both two structures. Moreover, for the band structure of hybrid lattice as shown in the middle of Fig. 1(b), the first band is similar to the honeycomb lattice, while the first flat band appears within the band gap. This allows for experimental observation of flat band modes. In general, when the frequency is lower than half of the plasma frequency, the propagation of electromagnetic wave is cut off inside the plasma column, and the energy band mainly depends on the geometric structure of the lattice. As the frequency increases to half of the plasma frequency, the surface plasmon resonance is activated, thus the flat band appears. This origin of flat band in plasma photonic crystal is stark contrast to conventional flat band systems where the fundamental properties are determined by the lattice structure. Therefore, the plasma frequency provides a variety of opportunities to control the band structure.

For the purpose of exploring the origin of the Dirac point in the triangular lattice, we further plot its dispersion near the high symmetric point K as shown in Fig. 2. The circles extracted from Fig. 1(b) show the band structure near the K point. It can be seen that there is an almost linear dispersion relationship. To describe this dispersion phenomenon quantitatively, we exploit the  $\mathbf{k} \cdot \mathbf{p}$  theory to derive the reduced Hamiltonian for the triangular lattice [43], as illustrated in Appendix A. Thus the eigenfrequencies of propagating modes depend linearly on the distance  $\Delta\mathbf{k}$  of the quasimomentum from the K point. Then the analytic dispersion relationship near the K point is shown as the red curve in Fig. 2(a), while the circles are the results of the finite-difference calculation. Generally, for the periodic triangular-lattice plasma photonic crystal, there is also linear dispersion near the Dirac point,

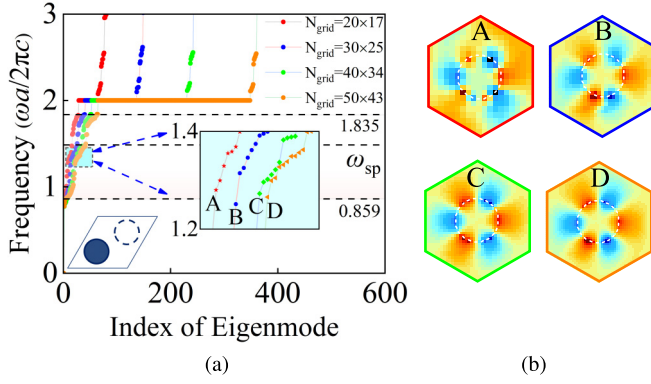


FIG. 3. Resolution dependence of the surface plasma mode. (a) Eigenfrequencies at high symmetric point  $\Gamma$  for TE modes computed with different grid resolutions for the triangular photonic crystal with  $\omega_{p0}a/2\pi c = 2$ . Red dots, blue dots, green dots, and orange dots correspond to the four resolutions of  $20 \times 17$ ,  $30 \times 25$ ,  $40 \times 34$ , and  $50 \times 43$ , respectively. The middle inset shows the eigenmode in the range of (1.2, 1.4), and the points A, B, C, and D are the lowest mode for this range. (b) The normal magnetic field distribution ( $H_z$ ) of a unit cell under four resolutions in the inset in (a), and the eigenfrequency  $\omega a/2\pi c$  is 1.280 for point A (upper left), 1.251 for point B (upper right), 1.272 for point C (lower left), and 1.266 for point D (lower right), respectively.

which is consistent with the trivial characteristics of dispersionless photonic crystals.

### III. STRUCTURE-INDEPENDENT LOCALIZATION BEHAVIOR

In this part, we focus on the properties of the dispersionless flat band modes which are presented in Fig. 1(b). The characteristics for dispersive bands are presented in the supplemental material [42].

The eigenfrequencies for TE modes versus the index of eigenmode with four different grid resolutions,  $N_{\text{grid}} = 20 \times 17$  (red dots),  $30 \times 25$  (blue dots),  $40 \times 34$  (green dots), and  $50 \times 43$  (orange dots), at the  $\Gamma$  point for a triangular lattice, are presented in Fig. 3(a). Furthermore, we also extracted the eigenmodes in the frequency range of (1.2, 1.4) as shown in the middle inset in Fig. 3(a), and the eigenfrequency  $\omega a/2\pi c$  in the inset is 1.280 for point A, 1.251 for point B, 1.272 for point C, and 1.266 for point D, respectively. The slight difference in the eigenfrequencies at these four points is due to the fact that the grid used is square. Figure 3(b) shows the magnetic field at four resolutions corresponding to points A (upper left), B (upper right), C (lower left), and D (lower right) in Fig. 3(a). It can be seen from Fig. 3(a) that the number of flat bands increases within the range of (0.859, 1.835) as the grid points increases. This implies that the flat band modes below  $\omega_{p0}a/2\pi c = 2$  are spatial oscillation modes (i.e., surface plasmon modes with a large wave number), which are only accessible to a grid scale smaller than the spatial oscillation scale, as shown in Fig. 3(b). Figure 3(b) exemplifies that the surface plasma mode becomes more apparent when the grid resolution increases from  $N_{\text{grid}} = 20 \times 17$  (upper left) to  $N_{\text{grid}} = 50 \times 43$  (bottom right). Furthermore, there are many

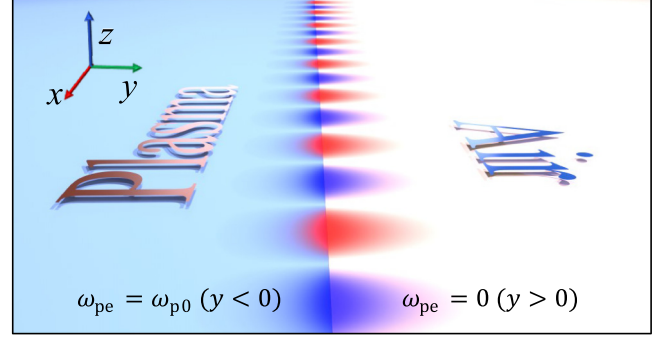


FIG. 4. Schematic diagram of the localization behavior of the magnetic field at the plasma-air interface. The region  $y > 0$  is air medium ( $\omega_{pe} = 0$ ), and the region  $y < 0$  is plasma medium ( $\omega_{pe} = \omega_{p0}$ ). The surface modes at the interface propagate along the  $x$  direction.

degenerate modes appear at  $\omega_{p0}a/2\pi c = 2$ , which are consistent with the number of grids in the plasma region. This degenerate behavior can be checked by the finite-difference matrix, and these modes describe the Langmuir oscillation (wave number is zero) in the plasma. The flat band illustrates the strong localization mode with almost zero group velocity and the extremely weak coupling of lattice sites. Specifically, for the modes below  $\omega_{p0}a/2\pi c = 2$ , the electromagnetic energy is localized at the interface between plasma and air and decays as an evanescent wave inside both sides of the interface. In order to investigate this localization mode, we consider the two-dimensional structure of the air half space ( $\omega_{pe} = 0$ ) for  $y > 0$  and the plasma filled half space ( $\omega_{pe} = \omega_{p0}$ ) for  $y < 0$ , as shown in Fig. 4. The electromagnetic wave propagates along the interface in the  $x$  direction and the magnetic field is polarized in the  $z$  direction. Considering the time harmonic dependence  $e^{i\omega t}$ , we combine Eq. (3) with Eq. (7) as the following equations:

$$i\omega H_z = -\frac{1}{\mu_0} \left( \frac{\partial E_y}{\partial x} - \frac{\partial E_x}{\partial y} \right), \quad (9)$$

$$\frac{\partial}{\partial y} \left( \frac{\partial E_y}{\partial x} - \frac{\partial E_x}{\partial y} \right) = \frac{1}{c^2} (\omega^2 - \omega_{pe}^2) E_x, \quad (10)$$

$$\frac{\partial}{\partial x} \left( \frac{\partial E_x}{\partial y} - \frac{\partial E_y}{\partial x} \right) = \frac{1}{c^2} (\omega^2 - \omega_{pe}^2) E_y. \quad (11)$$

Assuming that  $H_z$  has the following form [44]:

$$H_z = \begin{cases} \frac{A_1}{\mu_0} e^{i\kappa x} e^{\beta_1 y}, & y < 0 \\ \frac{A_2}{\mu_0} e^{i\kappa x} e^{-\beta_2 y}, & y > 0 \end{cases}. \quad (12)$$

The parameter  $\kappa$  refers to the propagation constant along the interface, and  $\beta_1$  and  $\beta_2$  are the attenuation coefficients in the plasma and air, respectively. Continuity of  $H_z$  at the interface requires that  $A_1 = A_2 = A$ , and, thus,

$$E_x = \begin{cases} -A \frac{i\omega}{\omega^2 - \omega_{p0}^2} \beta_1 e^{i\kappa x} e^{\beta_1 y}, & y < 0 \\ A \frac{i}{\omega} \beta_2 e^{i\kappa x} e^{-\beta_2 y}, & y > 0 \end{cases} \quad \text{and} \quad (13)$$

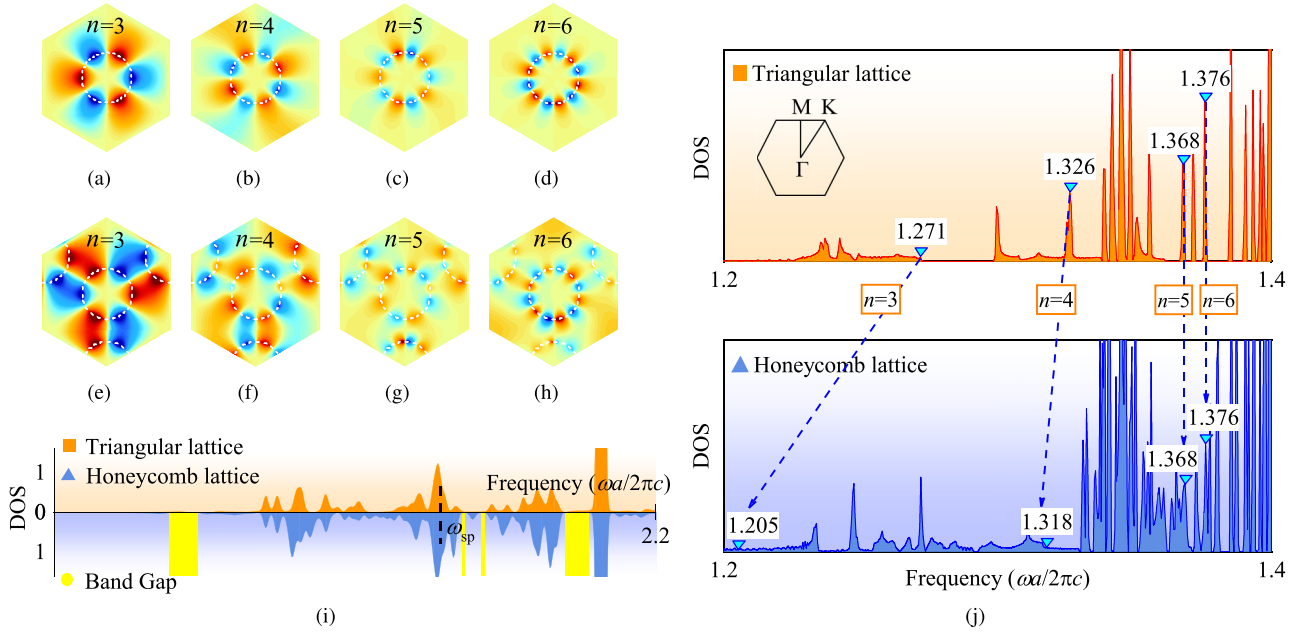


FIG. 5. The normal magnetic field ( $H_z$ ) profiles in magnitude for different surface plasmon modes and the DOS distribution of TE polarization for the triangular lattice and honeycomb lattice. Panels (a)–(d) and (e)–(h) present the magnetic field distribution with  $n = 3, 4, 5, 6$  at the  $\Gamma$  point in the first Brillouin zone of the triangular lattice and honeycomb lattice, respectively. The grid resolution is  $N_{\text{grid}} = 300 \times 259$ . Panel (i) presents the DOS of the two lattices. Panel (j) is extracted from panel (i): The upper represents the triangular lattice and the lower represents the honeycomb lattice.

$$E_y = \begin{cases} -A \frac{\omega}{\omega^2 - \omega_{p0}^2} \kappa e^{i\kappa x} e^{\beta_1 y}, & y < 0 \\ -A \frac{1}{\omega} \kappa e^{i\kappa x} e^{-\beta_2 y}, & y > 0 \end{cases}. \quad (14)$$

According to the continuity of  $E_x$  at the interface, we obtain the following relationship:

$$\frac{\beta_2}{\beta_1} = -\frac{\omega^2}{\omega^2 - \omega_{p0}^2}. \quad (15)$$

By substituting  $E_x$  and  $E_y$  into Eq. (10) or Eq. (11), we can get:

$$\beta_1^2 = \kappa^2 - \frac{1}{c^2} (\omega^2 - \omega_{p0}^2) \quad (16)$$

and

$$\beta_2^2 = \kappa^2 - \frac{1}{c^2} \omega^2. \quad (17)$$

According to Eqs. (15)–(17), the propagation constant at the interface can be expressed as:

$$\kappa = \frac{1}{c} \sqrt{\frac{2\omega^2(\omega^2 - \omega_{p0}^2)}{2\omega^2 - \omega_{p0}^2}}. \quad (18)$$

The surface plasmon modes at the circularly symmetric interface between the plasma and air exhibit quantized wave numbers due to the boundary condition imposed by the geometry. When  $n$  azimuthally periodic repetitions are considered on the circle, it possesses translation symmetry in the azimuthal direction with a period of  $2\pi/n$ . Thus,  $\kappa = n/r$ ,

where the integer azimuthal mode number  $n = 1, 2, 3, \dots$ . As  $n$  approaches infinity, we can get the frequency of surface plasmon oscillation  $\omega_{\text{sp}} = \frac{1}{\sqrt{2}} \omega_{p0}$ , which is marked in Figs. 3(a).

Figure 5 shows the magnetic fields in magnitude for four azimuthal mode numbers  $n = 3, 4, 5$  and  $6$  in two lattices at the point  $\Gamma$  below the surface plasma frequency  $\omega_{\text{sp}}$ . The deviation of numerical calculation of the field distribution shown in Fig. 5 essentially came from the localized nature of the eigenmodes of the surface plasmon modes. Therefore, the field distribution is difficult to reproduce by the discretization of a small number of sample points. It can be seen that the electromagnetic energy is strongly localized on the surface of the plasma column, which is in contrast to the low-frequency case (Figs. S2 and S3 in the Supplemental Material [42]) where the energy is dispersed in the air. This is due to the decaying of the magnetic field of the surface plasmon polarization on both sides of the interface as described in Eq. (12). Meanwhile, the group velocity is close to zero, resulting in the flat band as shown in Fig. 1(b). Furthermore, the flat band represents high density of states. Figure 5(i) describes the DOS of triangular lattice (orange plot) and honeycomb lattice (blue plot). The band gap is marked with yellow. For  $n = 3$  modes shown in Figs. 5(a) and 5(e), the magnetic field has three local maxima along the angular direction. There exists a pronounced coupling between the sites of the honeycomb lattice compared to the triangular lattice, which results in an inconsistency in their eigenfrequencies. As shown in Figs. 5(j), when  $n = 3$ , the eigenfrequency for the triangular lattice is 1.271, while it is 1.205 for the honeycomb lattice. However, this inconsistent tendency on the eigenfrequencies is decreasing with the increasing  $n$  as shown in Figs. 5(j). Since the localization

behavior becomes obvious for larger  $n$  and the coupling between the sites is weakened, the dependence of eigenfrequency on the lattice structure decreases. For example, when  $n = 5$  and  $n = 6$  as shown in Fig. 5, both lattices present the identical eigenfrequencies (1.368 for  $n = 5$  and 1.376 for  $n = 6$ ). For larger modes, the predicted eigenfrequencies shall have a rising tendency of approaching  $\omega_{\text{sp}}$ , as illustrated in Figs. 3(a). Therefore, a large amount of modes will accumulate near  $\omega_{\text{sp}}$ , and thus a DOS peak appears, as shown in Figs. 5(i).

#### IV. CONCLUSION

In summary, we have theoretically investigated the energy band and eigenmodes of a typical TE polarized triangular and honeycomb lattice consisting of lossless dispersion plasma columns embedded in air. Specifically, by simplifying the governing equations of a TE polarized dispersion system, we deduce the Hermitian eigenstates of the vector electric field. It is found that there are dispersive bands and nondispersive energy bands at the specific frequency range in these two kinds of lattices. For instance, there exists a band gap in the honeycomb lattice while a double degeneracy occurs at K point in the triangular lattice. Since the energy concentrates on the air host, these band characteristics are strongly dependent on the crystal structure. However, for the surface plasmon-induced flat band, it exhibits the strong localization of the energy at the interface of the plasma and air with almost zero group velocity, which produces the extremely weak coupling between the lattice sites and thus results in the structure-independent eigenfrequencies. Our findings on such plasma frequency-dependent localization at the interface offer a way to implement a robust flat band characteristic immune to the lattice disorder. Moreover, the analytic research of the flat band in the dispersive photonic crystals system provides a new freedom to realize the specific control of the band structure.

#### ACKNOWLEDGMENT

This work is supported by the National Natural Science Foundation of China (NSFC Grants No. 12175050 and No. 12205067).

#### APPENDIX

The governing equation Eq. (7) for the TE modes can be rewritten as:

$$\nabla(\nabla \cdot \mathbf{E}) - \nabla^2 \mathbf{E} + \frac{\omega_{\text{pe}}^2}{c^2} \mathbf{E} = \frac{\omega^2}{c^2} \mathbf{E}. \quad (\text{A1})$$

Since point K is a high symmetry point and the energy band is degenerate at point K, forming a Dirac cone, thus point K is suitable as the  $k_0$  point to study the dispersion relation of the Dirac cone. According to Fig. 1(a), the eigenfrequency at point K is 0.553. By utilizing the Bloch theorem, one can get the wave function at the wave vector  $\mathbf{k}$  near a selected  $\mathbf{k}_0$  as follows:

$$\mathbf{E}_{nk} = e^{i(\mathbf{k}-\mathbf{k}_0)\cdot\mathbf{r}} \sum_j \alpha_{nj}(\mathbf{k}) \cdot \mathbf{E}_{jk_0}. \quad (\text{A2})$$

where  $n$  is the band number and  $\alpha_{nj}(\mathbf{k})$  is the expanding coefficient of the  $E_x$  and  $E_y$ . The wave function  $\mathbf{E}_{jk_0}$  at  $\mathbf{k}_0$  point can be obtained numerically. Then substituting Eq. (A2) into Eq. (A1),

$$\begin{aligned} \nabla(\nabla \cdot \mathbf{E}) &= e^{i(\mathbf{k}-\mathbf{k}_0)\cdot\mathbf{r}} \sum_j \alpha_{nj}(\mathbf{k}) \left\{ -(\mathbf{k}-\mathbf{k}_0)[(\mathbf{k}-\mathbf{k}_0) \cdot \mathbf{E}_{jk_0}] \right. \\ &\quad \left. + i\nabla[(\mathbf{k}-\mathbf{k}_0) \cdot \mathbf{E}_{jk_0}] + i(\mathbf{k}-\mathbf{k}_0)\nabla \cdot \mathbf{E}_{jk_0} \right. \\ &\quad \left. + \nabla(\nabla \cdot \mathbf{E}_{jk_0}) \right\} \end{aligned} \quad (\text{A3})$$

and

$$\begin{aligned} \nabla^2 \mathbf{E} &= e^{i(\mathbf{k}-\mathbf{k}_0)\cdot\mathbf{r}} \sum_j \alpha_{nj}(\mathbf{k}) \left[ -|\mathbf{k}-\mathbf{k}_0|^2 \mathbf{E}_{jk_0} \right. \\ &\quad \left. + 2i\nabla(\mathbf{k}-\mathbf{k}_0) \cdot \nabla \mathbf{E}_{jk_0} + \nabla^2 \mathbf{E}_{jk_0} \right]. \end{aligned} \quad (\text{A4})$$

Finally, we obtain

$$\begin{aligned} e^{i(\mathbf{k}-\mathbf{k}_0)\cdot\mathbf{r}} \sum_j \alpha_{nj}(\mathbf{k}) \left\{ -(\mathbf{k}-\mathbf{k}_0)[(\mathbf{k}-\mathbf{k}_0) \cdot \mathbf{E}_{jk_0}] \right. \\ \left. + i\nabla(\mathbf{k}-\mathbf{k}_0) \cdot \nabla \mathbf{E}_{jk_0} + i\nabla(\mathbf{k}-\mathbf{k}_0)[\nabla \cdot \mathbf{E}_{jk_0}] \right. \\ \left. - 2i\nabla(\mathbf{k}-\mathbf{k}_0) \cdot \nabla \mathbf{E}_{jk_0} + \frac{\omega_{jk_0}^2 - \omega_{nk}^2}{c^2} \mathbf{E}_{jk_0} \right\} = 0. \end{aligned} \quad (\text{A5})$$

Using the orthogonal regime of the wave function  $\mathbf{E}_{jk_0}$  and  $\mathbf{E}_{lk_0}$  as presented in Eq. (8), where the integral area is the unit cell of the triangular lattice, Eq. (A5) can be rewritten as:

$$\sum_j \alpha_{nj}(\mathbf{k}) \left[ P_{lj}(\mathbf{k}) - \frac{\omega_{nk}^2 - \omega_{jk_0}^2}{c^2} \delta_{lj} \right] = 0, \quad (\text{A6})$$

where

$$P_{lj}(\mathbf{k}) = \Delta \mathbf{k} \cdot \mathbf{p}_{lj} + \Delta k_x \Delta k_y h_{lj} + |\Delta \mathbf{k}|^2 q_{lj}, \quad (\text{A7})$$

with

$$\mathbf{p}_{lj} = i \int d\mathbf{r} \left[ \mathbf{E}_{lk_0}^* \cdot \nabla \mathbf{E}_{jk_0} + \mathbf{E}_{lk_0}^* (\nabla \cdot \mathbf{E}_{jk_0}) - 2\nabla \mathbf{E}_{jk_0} \cdot \mathbf{E}_{lk_0}^* \right], \quad (\text{A8})$$

$$h_{lj} = - \int d\mathbf{r} \mathbf{E}_{lk_0}^* \sigma \mathbf{E}_{jk_0}, \quad (\text{A9})$$

and

$$q_{lj} = \delta_{lj}. \quad (\text{A10})$$

Here  $\Delta \mathbf{k} = \mathbf{k} - \mathbf{k}_0$ ,  $\sigma = \begin{pmatrix} 0 & 1 \\ 1 & 0 \end{pmatrix}$ . It is obvious that  $P_{lj}(\mathbf{k}) = P_{jl}^*(\mathbf{k})$ , thus the Hermitian matrix  $P_{lj}(\mathbf{k})$  can be regarded as a reduced Hamiltonian, namely

$$H_{lj} = P_{lj}(\mathbf{k}). \quad (\text{A11})$$

To obtain a nontrivial eigensolution of Eq. (A6), then

$$\det \left| H - \frac{\omega_{nk}^2 - \omega_{jk_0}^2}{c^2} I \right| = 0. \quad (\text{A12})$$

When considering the linear dispersion relation at the degenerate point in the band structure of the triangular lattice, the nonlinear terms  $\Delta k_x \Delta k_y h_{lj}$  and  $|\Delta \mathbf{k}|^2 q_{lj}$  in Eq. (A7) are

ignored and only the linear term  $\Delta\mathbf{k} \cdot \mathbf{p}_{lj}$  is retained. Consequently, we only need to consider the degenerate states at the Dirac point in the summation of Eq. (A2). Thus, the  $2 \times 2$  reduced Hamiltonian at the K point can be numerically calculated. According to the definition of  $\mathbf{p}_{lj}$  in Eq. (A8), the following equations can be obtained:

$$\mathbf{p}_{11} = -\mathbf{p}_{22}, \quad (\text{A13})$$

$$\mathbf{p}_{12}^* = \mathbf{p}_{21}, \quad (\text{A14})$$

$$|\mathbf{p}_{11}|_{x/y} = |\mathbf{p}_{12}|_{x/y}, \quad (\text{A15})$$

$$\mathbf{p}_{11,x/y} \cdot \mathbf{p}_{12,x/y} = 0. \quad (\text{A16})$$

From Eq. (A12), we can approximate the dispersion relationship at the K point as follows:

$$\omega = \omega_0 + \frac{c^2 \sqrt{|\Delta\mathbf{k} \cdot \mathbf{p}_{11}|^2 + |\Delta\mathbf{k} \cdot \mathbf{p}_{12}|^2}}{2\omega_0}, \quad (\text{A17})$$

where  $\omega_0 a/2\pi c = 0.544$  is the eigenfrequency of the degenerate modes. Combining Eq. (A15) and Eq. (A16), we can obtain an isotropic linear dispersion relation, which can be seen in Fig. 2(b).

- 
- [1] M. Wu, Z. Li, T. Cao, and S. G. Louie, Physical origin of giant excitonic and magneto-optical responses in two-dimensional ferromagnetic insulators, *Nat. Commun.* **10**, 2371 (2019).
- [2] V. Peri, Z.-D. Song, B. A. Bernevig, and S. D. Huber, Fragile Topology and Flat-band Superconductivity in the Strong-coupling Regime, *Phys. Rev. Lett.* **126**, 027002 (2021).
- [3] Z. Liu, G. Wei, D. Zhang, W. Chen, L. Sun, J. Li, and J. J. Xiao, Strong frequency-dependent beam steering dynamics, Zitterbewegung effect, and Klein tunneling in a ternary plasmonic-dielectric superlattice, *Phys. Rev. B* **103**, 195415 (2021).
- [4] S. Islam, S. Bhattacharyya, H. Nhalil, S. Elizabeth, and A. Ghosh, Signature of pseudodiffusive transport in mesoscopic topological insulators, *Phys. Rev. Res.* **2**, 033019 (2020).
- [5] S. Weidemann, M. Kremer, S. Longhi, and A. Szameit, Topological triple phase transition in non-hermitian Floquet quasicrystals, *Nature (London)* **601**, 354 (2022).
- [6] K. Merkel, M. Panhans, S. Hutsch, and F. Ortmann, Interplay of band occupation, localization, and polaron renormalization for electron transport in molecular crystals: Naphthalene as a case study, *Phys. Rev. B* **105**, 165136 (2022).
- [7] A. Cerjan, S. Huang, M. Wang, K. P. Chen, Y. Chong, and M. C. Rechtsman, Experimental realization of a Weyl exceptional ring, *Nat. Photon.* **13**, 623 (2019).
- [8] S. Yves, T. Berthelot, M. Fink, G. Lerosey, and F. Lemoult, Measuring Dirac Cones in a Subwavelength Metamaterial, *Phys. Rev. Lett.* **121**, 267601 (2018).
- [9] B.-Y. Xie, G.-X. Su, H.-F. Wang, H. Su, X.-P. Shen, P. Zhan, M.-H. Lu, Z.-L. Wang, and Y.-F. Chen, Visualization of Higher-order Topological Insulating Phases in Two-Dimensional Dielectric Photonic Crystals, *Phys. Rev. Lett.* **122**, 233903 (2019).
- [10] S. Wu, B. Jiang, Y. Liu, and J.-H. Jiang, All-dielectric photonic crystal with unconventional higher-order topology, *Photon. Res.* **9**, 668 (2021).
- [11] G. Hu, Q. Ou, G. Si, Y. Wu, J. Wu, Z. Dai, A. Krasnok, Y. Mazon, Q. Zhang, Q. Bao, C.-W. Qiu, and A. Alù, Topological polaritons and photonic magic angles in twisted  $\alpha$ -MoO<sub>3</sub> bilayers, *Nature (London)* **582**, 209 (2020).
- [12] J. D. Joannopoulos, S. G. Johnson, J. N. Winn, and R. D. Meade, *Photonic Crystals: Molding the Flow of Light* (Princeton University Press, Princeton, NJ, 2008).
- [13] J. D. Joannopoulos, P. R. Villeneuve, and S. Fan, Photonic crystals: Putting a new twist on light, *Nature (London)* **386**, 143 (1997).
- [14] F. R. Prudêncio and M. G. Silveirinha, Ill-Defined Topological Phases in Local Dispersive Photonic Crystals, *Phys. Rev. Lett.* **129**, 133903 (2022).
- [15] M. G. Silveirinha, Proof of the Bulk-Edge Correspondence Through a Link Between Topological Photonics and Fluctuation-Electrodynamics, *Phys. Rev. X* **9**, 011037 (2019).
- [16] M. R. Bourgeois, A. W. Rossi, S. Khorasani, and D. J. Masiello, Optical control over thermal distributions in topologically trivial and non-trivial plasmon lattices, *ACS Photon.* **9**, 3656 (2022).
- [17] S. Bharadwaj, T. Van Mechelen, and Z. Jacob, Picophotonics: Anomalous Atomistic Waves in Silicon, *Phys. Rev. Appl.* **18**, 044065 (2022).
- [18] A. Raman and S. Fan, Photonic Band Structure of Dispersive Metamaterials Formulated as a Hermitian Eigenvalue Problem, *Phys. Rev. Lett.* **104**, 087401 (2010).
- [19] W. Xiao, B. Gong, J. Sun, and Z. Zhang, Finite element calculation of photonic band structures for frequency dependent materials, *J. Sci. Comput.* **87**, 27 (2021).
- [20] K. S. Novoselov, A. K. Geim, S. V. Morozov, D. Jiang, Y. Zhang, S. V. Dubonos, I. V. Grigorieva, and A. A. Firsov, Electric field effect in atomically thin carbon films, *Science* **306**, 666 (2004).
- [21] A. H. Castro Neto, F. Guinea, N. M. R. Peres, K. S. Novoselov, and A. K. Geim, The electronic properties of graphene, *Rev. Mod. Phys.* **81**, 109 (2009).
- [22] S.-G. Lee, S.-H. Kim, and C.-S. Kee, Band dynamics accompanied by bound states in the continuum at the third-order  $\gamma$  point in leaky-mode photonic lattices, *Photon. Res.* **9**, 1109 (2021).
- [23] B. Zhen, C. W. Hsu, Y. Igarashi, L. Lu, I. Kaminer, A. Pick, S.-L. Chua, J. D. Joannopoulos, and M. Soljačić, Spawning rings of exceptional points out of Dirac cones, *Nature (London)* **525**, 354 (2015).
- [24] D. I. Vulis, O. Reshef, P. Camayd-Muñoz, and E. Mazur, Manipulating the flow of light using Dirac-cone zero-index metamaterials, *Rep. Prog. Phys.* **82**, 012001 (2019).
- [25] K. Wang, Dirac cones in isogonal hexagonal metallic structures, *Phys. Rev. B* **97**, 125146 (2018).
- [26] S. Bittner, B. Dietz, M. Miski-Oglu, and A. Richter, Extremal transmission through a microwave photonic crystal and the observation of edge states in a rectangular Dirac billiard, *Phys. Rev. B* **85**, 064301 (2012).
- [27] X. Li, E. Zhao, and W. V. Liu, Topological states in a ladder-like optical lattice containing ultracold atoms in higher orbital bands, *Nat. Commun.* **4**, 1523 (2013).

- [28] M. Mirhosseini, E. Kim, V. S. Ferreira, M. Kalaei, A. Sipahigil, A. J. Keller, and O. Painter, Superconducting metamaterials for waveguide quantum electrodynamics, *Nat. Commun.* **9**, 3706 (2018).
- [29] K. Dong, T. Zhang, J. Li, Q. Wang, F. Yang, Y. Rho, D. Wang, C. P. Grigoropoulos, J. Wu, and J. Yao, Flat Bands in Magic-Angle Bilayer Photonic Crystals at Small Twists, *Phys. Rev. Lett.* **126**, 223601 (2021).
- [30] M. Kang, S. Fang, L. Ye, H. C. Po, J. Denlinger, C. Jozwiak, A. Bostwick, E. Rotenberg, E. Kaxiras, J. G. Checkelsky, and R. Comin, Topological flat bands in frustrated kagome lattice CoSn, *Nat. Commun.* **11**, 4004 (2020).
- [31] L. Balents, C. R. Dean, D. K. Efetov, and A. F. Young, Superconductivity and strong correlations in moiré flat bands, *Nat. Phys.* **16**, 725 (2020).
- [32] Y. Choi, J. Kemmer, Y. Peng, A. Thomson, H. Arora, R. Polski, Y. Zhang, H. Ren, J. Alicea, G. Refael, F. von Oppen, K. Watanabe, T. Taniguchi, and S. Nadj-Perge, Electronic correlations in twisted bilayer graphene near the magic angle, *Nat. Phys.* **15**, 1174 (2019).
- [33] P. A. Belov, C. R. Simovski, and P. Ikonen, Canalization of subwavelength images by electromagnetic crystals, *Phys. Rev. B* **71**, 193105 (2005).
- [34] S. Mukherjee, M. Di Liberto, P. Öhberg, R. R. Thomson, and N. Goldman, Experimental Observation of Aharonov-Bohm Cages in Photonic Lattices, *Phys. Rev. Lett.* **121**, 075502 (2018).
- [35] S. Longhi, Photonic flat-band laser, *Opt. Lett.* **44**, 287 (2019).
- [36] Z. Li, Mesoscopic and microscopic strategies for engineering plasmon-enhanced raman scattering, *Adv. Opt. Mater.* **6**, 1701097 (2018).
- [37] S. Zhang, X. Lu, and J. Liu, Correlated Insulators, Density Wave States, and Their Nonlinear Optical Response in Magic-Angle Twisted Bilayer Graphene, *Phys. Rev. Lett.* **128**, 247402 (2022).
- [38] D. Leykam, A. Andreanov, and S. Flach, Artificial flat band systems: From lattice models to experiments, *Adv. Phys.: X* **3**, 1473052 (2018).
- [39] S. Mukherjee, A. Spracklen, D. Choudhury, N. Goldman, P. Öhberg, E. Andersson, and R. R. Thomson, Observation of a Localized Flat-Band State in a Photonic Lieb Lattice, *Phys. Rev. Lett.* **114**, 245504 (2015).
- [40] L. Tang, D. Song, S. Xia, S. Xia, J. Ma, W. Yan, Y. Hu, J. Xu, D. Leykam, and Z. Chen, Photonic flat-band lattices and unconventional light localization, *Nanophotonics* **9**, 1161 (2020).
- [41] C. Cantillano, S. Mukherjee, L. Morales-Inostroza, B. Real, G. Cáceres-Aravena, C. Hermann-Avigliano, R. R. Thomson, and R. A. Vicencio, Observation of localized ground and excited orbitals in graphene photonic ribbons, *New J. Phys.* **20**, 033028 (2018).
- [42] See Supplemental Material at <http://link.aps.org/supplemental/10.1103/PhysRevB.107.195301> for the characteristics of the lower frequency modes; comparison of the surface plasmon modes between the isolated plasma rod and two photonic crystals; perturbation analysis of eigenfrequencies in the presence of weak dissipation.
- [43] J. Mei, Y. Wu, C. T. Chan, and Z.-Q. Zhang, First-principles study of Dirac and Dirac-like cones in phononic and photonic crystals, *Phys. Rev. B* **86**, 035141 (2012).
- [44] S. A. Maier *et al.*, *Plasmonics: Fundamentals and Applications*, Vol. 1 (Springer, Berlin, 2007).